Contactless Voltage Measurement Considering Spatially Dependent Voltage Compensation

Yuxiang Leng, Liang Shu,* Qi Qian, Chong Chen, and Yigang Lin

Low Voltage Apparatus Technology Research Center of Zhejiang, Wenzhou University,
261 Wei Seventeen Road, Wengyang Street, Yueqing, Zhejiang Province 325600, China

The measurement accuracy and stability of a contactless voltage sensor are greatly affected by the relative locations of the cable and sensor. We propose a contactless voltage sensing method considering the adaptive compensation of the induced voltage of an electrode array to improve the sensing accuracy and reliability. A novel electrode array structure composed of four uniformly distributed electrodes is designed to collect the spatially distributed electric field around the power cable. To quantify the correlation between the change in the relative location of the cable and the induced voltage of the electrode array, a setup for measuring sensor output characteristics based on the coordinated control of dual motors and the synchronous collection of induced voltages of electrodes is developed. The relationship between the change in cable location and the sensing voltage is studied at different voltages. To further improve the sensing accuracy, a voltage adaptive compensation method is proposed, in which a linear regression algorithm is used to analyze and learn the quantitative relationship between the induced voltage of the electrode array and the cable location. The results of a verification test carried out in the range of 160–240 V AC show that by voltage adaptive compensation, the voltage fluctuation range caused by the change in the relative location of the cable is reduced from ±25 to ±4 V and the maximum measurement error is reduced from 15% to less than 2.5%.

1. Introduction

Voltage measurement with high accuracy and reliability is critical for collecting system operating information and a fundamental requirement for power system monitoring and diagnosis. There are two main methods of voltage measurement: contact voltage measurement and contactless voltage measurement.[1] At present, traditional electric energy information collection terminals are designed on the basis of contact voltage measurement, which requires the metal part of the cable to be led out or placed in contact with an intrusive measuring probe.[2] Thus, the probe can be connected to a secondary device for voltage and current measurements. There are two main disadvantages of this methodology: (1) Installation is difficult. Because

---

traditional contact voltage measurement requires the copper core to be placed in contact with the measuring probe after destroying the insulation layer of the cable, the primary side must be powered off for installation, which affects the quality of the power supply. (2) There are serious potential safety hazards. During the contact measurement, the insulation layer of the cable is damaged, and the operation safety of power cables and equipment faces a severe challenge including the risk of electrical leakage. Contactless voltage measurement can avoid damage to the insulating layer. At present, there are two main methods of contactless voltage sensing: photoelectric sensing and electric field coupling sensing. Photoelectric sensing technology is based on the optical principles used for voltage measurement.[3] Optical materials are usually used to detect spatial electric fields, then the detected fields are converted into voltage measurements. This method has good measurement accuracy, but the cost of optical materials is usually very high and the sensing results tend to be affected by ambient light.[4]

Contactless voltage measurement based on electric field coupling is more convenient for use in industry. The basic principle is that by applying a certain voltage or electric field, an electromotive force will be induced on the induction electrodes, and resistance or capacitive connections can be formed between electrodes. The voltage induced by the electrodes can be collected. After applying a suitably designed algorithm, the induced electrode voltage can be used to calibrate the applied voltage.[5] Different studies of contactless voltage sensors have been conducted on the basis of this principle. In Ref. 6, the design and implementation details of a complete noncontact voltage acquisition system that allows the measurement of power-line voltage waveforms without galvanic contact were presented. In Ref. 7, a capacitive noncontact ac voltage measurement technique and its feasibility for measuring arbitrary waveform signals were analyzed. Several errors related to the technique were analyzed to show the impact of different design parameters on the final accuracy. To optimize the design, different sensor structures for different sensing purposes have been studied. In Ref. 8, a system of differential-output monitors that diagnose current and voltage in the vacuum section of a 20 MA, 3 MV pulsed-power accelerator was developed. The pair of opposite-polarity structures in the system was designed to provide a differential output. In Ref. 9, a three-electrode sensor was designed, with the electrodes located in a ring to improve the electric field distribution, insulation performance, and sensor sensitivity. In Ref. 5, the operating principle, design, and testing of a coaxial D-dot (time derivative of electric flux density) probe to measure fast-front high voltages were presented. The designed coaxial three-electrode ring was improved and applied to the measurement of very fast transient voltages.

Since contactless voltage measurement is implemented without galvanic contact, the sensing performance could be affected by external interference or environmental factors. In Ref. 10, a probe design that could be calibrated in situ each time the probe was moved was described. This probe design with automatic calibration could be used to account for both the locational sensitivity and the tested device dependence. In Ref. 11, an improved technique for the accurate contactless measurement of absolute voltage waveforms of microwave circuits was proposed. An

electromagnetic model was used in the improved technique to extract the variation of the coupling capacitance with the frequency.

Another method of improving sensing performance is self-correction. In Ref. 12, a smart meter for power consumption based on a capacitive coupling design that could measure both current and voltage without any physical contact with the electric load was developed. A calibration algorithm with two preprocessing channels for self-calibration to provide accurate measurements regardless of the cable type was proposed. In Ref. 13, a low-cost wireless voltage sensor was developed for medium- and high-voltage (MV/HV) utility assets. An algorithm for sensing the moving average voltage was proposed and tested using simulations and validated using a high-voltage prototype. In Ref. 14, a resin-molded voltage–current waveform sensor for measuring the power factor and harmonics in power distribution systems was proposed and prototyped. Numerical electromagnetic analysis was executed using the finite element method to estimate the characteristics and behaviors of the sensor. In Ref. 15, methods for the contactless measurement of instantaneous voltage and for waveform reconstruction were presented. Voltage waveforms were reconstructed by an artificial neural network to improve the sensing accuracy. In Ref. 16, a capacitive probe with two sensor heads was developed for the accurate sensing of ac voltage. The orthogonal least-squares estimation algorithm was implemented to identify the nonlinear relationship between the readings of the two sensor heads and the sensed ac voltage. The sensing signal was then reconstructed from the relationship model and the collected signals.

The basic principle of contactless measurement of the voltage is to collect the electric-field-dependent charge using a specially designed sensing probe. It is known from Helmholtz theory that the power-line-induced electric field is spatially distributed, and this distribution could affect the integration of the electric field to generate the corresponding probe charge. The sensing accuracy is greatly dependent on the relative locations of the power line and probe. Analyzing the sensing performance for different locations and performing voltage compensation are effective ways for ensuring the accuracy and reliability of contactless sensing. However, there is no mention of such an approach in the literature.

To improve sensing accuracy, a contactless voltage sensing method considering spatially dependent voltage compensation is proposed in this paper. A new electrode array structure composed of four uniformly distributed electrodes is designed to collect the spatially distributed electric field induced by a power line. To quantify the correlation between the change in the relative location of a cable and the voltage induced by an electrode array, a setup for measuring sensor output characteristics based on the coordinated control of dual motors and the synchronous collection of induced voltages of electrodes is developed. The relationship between the change in cable location and the sensing voltage is studied at different voltages. To further improve the accuracy of the sensing voltage, adaptive voltage compensation based on a linear regression algorithm to compensate for the sensing error resulting from the change in cable location is proposed. The proposed method of adaptive voltage compensation based on a linear regression algorithm is verified at voltages ranging from 160 to 240 V AC, and the measurement error was reduced from 15% before compensation to less than 2.5% after compensation.

2. Contactless Voltage Sensor

2.1 Principle of voltage sensing

An electric field is always induced around a power cable carrying an alternating current. The intensity of the induced electric field is proportional to the cable potential. If sensing electrodes are placed in such a field, a voltage can be induced from the electrodes, which can be used to calibrate the power-line voltage by applying a suitably designed algorithm. This principle is shown in Fig. 1.

The sensing electrode is placed at a location where the electric field intensity is E_0. According to the principle of electrostatic induction, a charge of q is induced on the surface of the metal electrode. If the electric field intensity changes over time, the induced charge will also change. The current generated by the changing charge flows through grounding resistor R, producing a voltage drop. This scenario satisfies the following equations:

$$q = \oint_A \varepsilon_0 E_0 dA,\tag{1}$$

$$V_0(t) = R_m \frac{dq}{dt} = \oint_A \varepsilon_0 \frac{dE_0}{dt} dA.\tag{2}$$

Here, q is the induced charge of the electrode, ε_0 is the dielectric constant in vacuum, E_0 is the electric field strength in the electrode placement space, A is the area of a closed Gaussian surface on the electrode surface, R_m is the grounding resistance of the electrode, and V_0 is the voltage drop caused by the current passing through the grounding resistance.

The relationship between the cable potential and the electric field intensity can be expressed as

$$\varphi_0 = \frac{1}{F} \cdot E_0,\tag{3}$$

where φ_0 is the cable potential and F is the scale factor between the cable potential and the electric field intensity, which is determined by the relative positions of the electrode and cable.
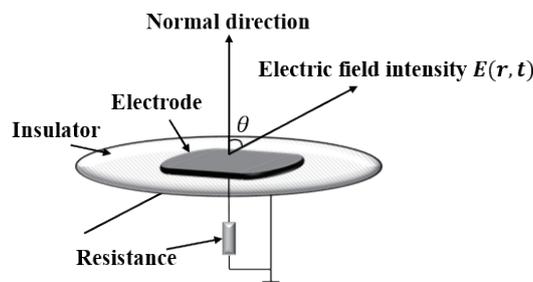

Fig. 1.   Principle of electric field coupling.

Combining Eqs. (2) and (3), we obtain

$$\varphi_0 = \frac{\int_0^t V_0 dt}{R_m \oint_A \varepsilon_0 F dA}. \qquad (4)$$

This is the relationship between the electrode voltage and the cable potential. Using this equation, the measured electrode voltage can be converted into the cable voltage to realize the contactless measurement of the cable voltage.

2.2 Structure of the sensor

The noncontact voltage sensor model proposed in this paper is shown in Fig. 2. The sensing area is a square of 15×15 mm^2. The role of the isolation baffle is to separate the cable and the sensing area, leaving an air gap between them. In contrast to a measurement method employing only a single electrode or a few electrodes, the electrode array design is able to capture the spatial distribution of the induced electric field, and changes in cable position can be predicted from variations of the voltage collected by the array. Such a design is helpful for voltage adaptive compensation if the cable is located in different positions. Our proposed contactless sensor structure and the electrode array are shown in Fig. 2, in which the coupling coils are designed to measure the cable current and the electrode array is designed to collect the induced voltage; a four-electrode structure with the four electrodes (A–D) uniformly distributed in a circle is employed.

The sensor consists of three main parts: an electrode array, a mutual inductance coil, and a sensing area. The mutual inductance coil is used for contactless current measurement. The area between the electrode array and the cable is the sensing area. Since the cable conductor need not be in contact with the electrode, the cable can be anywhere in the sensing area (Fig. 3). According to Helmholtz theory, when the relative position of the conductor changes, the voltage induced from the fixed electrode will change accordingly, leading to significant measurement errors. To improve the reliability and accuracy of sensing, such errors must be adaptively compensated for.
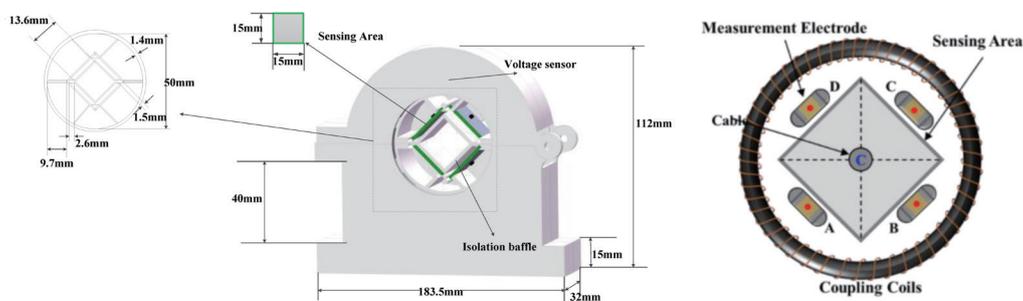

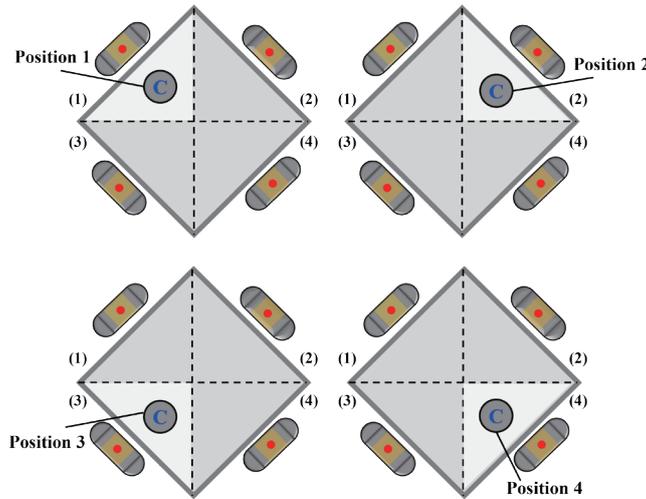Fig. 2.   (Color online) Sensor structure and electrode array.

Fig. 3.   (Color online) Different cable locations in the sensing area.

3.   Evaluation of Sensor Output Characteristics

To compensate for the errors, the sensor output characteristics corresponding to different cable positions must first be investigated. A setup for measuring output characteristics and the corresponding control method for the contactless voltage sensor are developed. The measurement setup and sensor prototype are shown in Fig. 4.

The cable position is controlled with two step motors, one to control the *x*-axis position and the other to control the *y*-axis position. The sensor is placed on a test bracket. The *x*-axis motor is connected to the sensor body through a linear screw rail and the *y*-axis motor is connected to the power line. The two motors are cooperatively controlled by a controller to drive the two linear screw rails to transmit displacements, and the cable can move along a specified path. The cable diameter is 1.6 mm. During the movement of the cable, a data acquisition (DAQ) system synchronously collects the data of both the cable location and the induced voltages of the electrodes to investigate the relationship between them. Four independent rail-to-rail operational amplifiers are designed for the DAQ system to amplify the electrode voltage. An LMV321 amplifier module is chosen since the chip channel is internally insulated, which is helpful for inhibiting the effect of mutual coupling between channels. An SYV75-9-type coaxial cable is chosen for signal transmission to decrease the effects of transmission coupling.

3.1   Motor control and path planning

To control the cable position, the cable must cover as much of the sensing area as possible. To facilitate the cooperative control of the dual motors, a suitable path for the cable is devised, as shown in Fig. 5, in which the dashed line represents the path moved by the cable and the arrow indicates the movement direction. From the start point, the cable moves back and forth in a serpentine shape between electrodes A and C while gradually moving from electrode B to
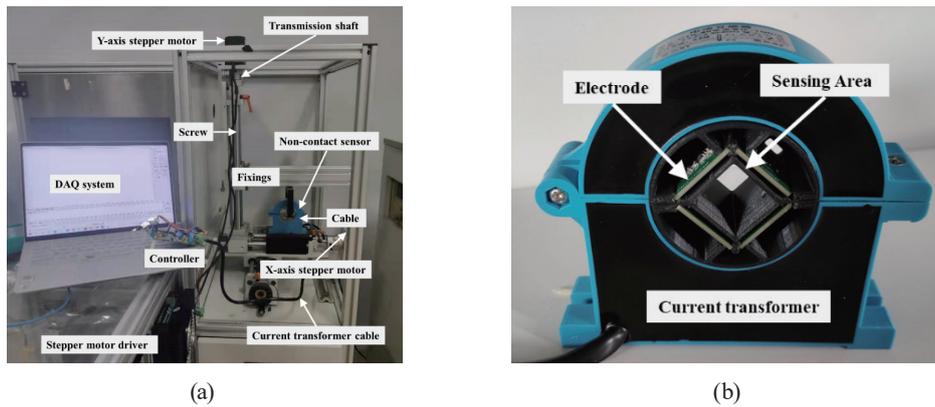
Fig. 4.   (Color online) Setup for measuring sensor characteristics and sensor prototype.
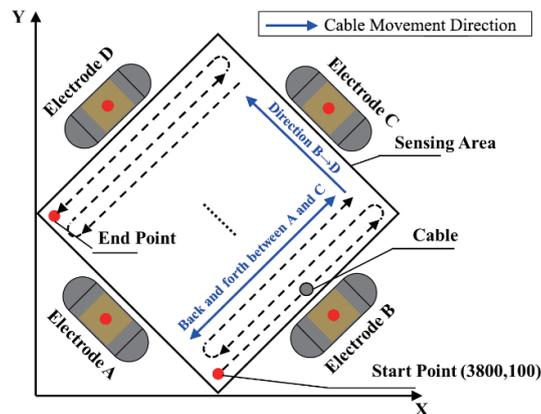

Fig. 5.   (Color online) Path of cable.

electrode D. Each time the cable reaches one of the 1446 sampling points along the path, the DAQ system simultaneously collects the corresponding cable location, the cable voltage, and the induced voltage of the four electrodes at this point.

The displacement of the cable is controlled by controlling the pulse of the two stepping motors. The positive rotation of the motors corresponds to an increase in the value of the encoder. In our design, the encoder value corresponds to the two motors, and the initial sampling point is set as (3800, 100). The two motors rotate at the same time to drive the two encoders to count, and when the change in the value of the encoder l is 100, the cable moves to the next sampling point. To avoid measurement errors due to time delay and cable vibration, the data collection is initiated 1 s after the cable reaches the sampling point. A flow chart of the motor control and data acquisition is shown in Fig. 6. From the start point to the end point, the cable reciprocates 19 times between electrodes A and C. Seventy-four sampling points are set on each reciprocating path with a distance of one sampling point between two adjacent reciprocating paths. Thus, there are 1446 sampling points in total. The change in the value of the encoder l
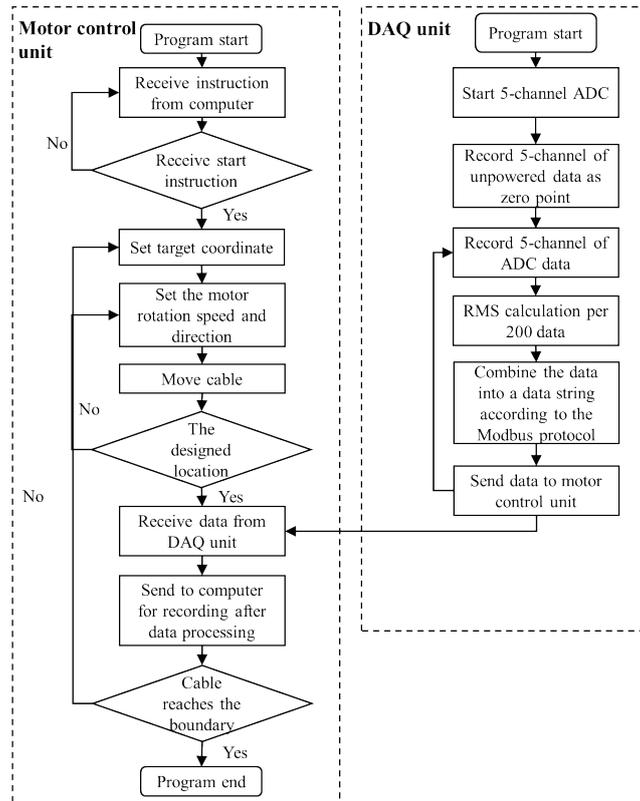
Fig. 6.   Flow chart of motor control and data acquisition.

indicates the distance between adjacent sampling points, which is 0.43 mm. The length of one reciprocating path is 32 mm and the distance between two adjacent paths is 0.86 mm.

3.2   Test data and error analysis

In our design, the power cable is tested with four different AC voltages (RMS values of 160, 180, 220, and 240 V) at different spatial locations, and four data sets are obtained, each of which contains 1446 items of data. The power frequency is 50 Hz. Part of the testing data, including the cable location and the four induced electrode voltages, are shown in Table 1 for the cable voltage of 240 V. Induced voltage variations corresponding to different cable locations are plotted in Fig. 7. Note that the magnitudes of the inducted potentials directly collected from the electrodes are only at the mV level. To facilitate data acquisition, an amplifier is designed for the controller to amplify the voltage to the V level. The *x*-axis represents the serial numbers of the 1446 sampling points and the *y*-axis represents the induced electrode voltage. The start and end points correspond to the blue dots shown in Fig. 5, and each collection point represents one of the cable locations in Fig. 5. It can be seen from Fig. 7 that when the cable moves from the start point to the end point, the induced voltages of electrodes A–D fluctuate significantly, making it difficult to accurately calibrate the cable voltage. By further comparing the induced voltage data of the

Table 1
Part of testing data including cable locations and induced voltages.

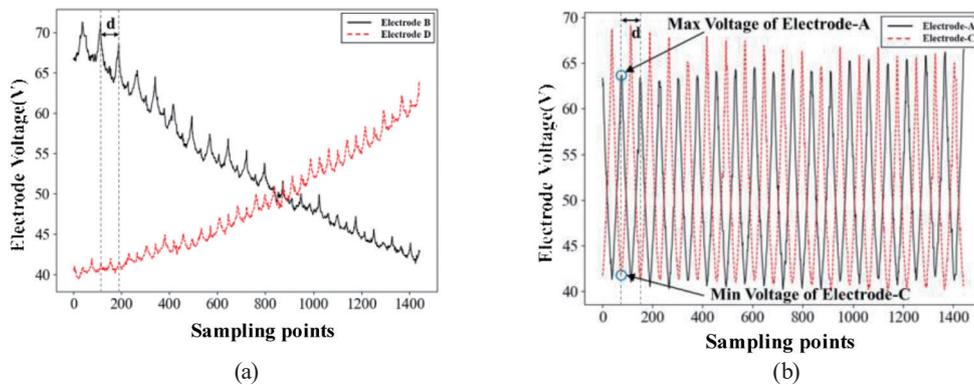| SN	Cable location		Electrode A (V)	Electrode B (V)	Electrode C (V)	Electrode D (V)	Cable voltage (V)
	x-axis	*y*-axis					
1	4.25	0.7	60.3	67	44	40.8	242.2
2	4.15	0.6	61.2	66.9	43.5	40.8	242.3
4	4.05	0.5	60.9	66.5	43.2	41	242.3
5	3.95	0.4	60.9	66.5	43.2	41	242.3
6	3.85	0.3	64	67	42.3	41.2	242.1
7	3.75	0.2	64.2	67.1	42.3	41.3	242
8	3.65	0.1	64.3	67.2	42.2	41.5	242.2
9	3.55	0.2	64	66.9	42.3	41.3	242.6

Fig. 7.   (Color online) Changes in induced voltages of electrodes when cable moves along path.

four electrodes, it is found that since the overall direction of the cable movement is from electrode B to electrode D, the voltage fluctuations of electrodes B and D are much larger than those of electrodes A and C. Because the cable undergoes cyclic reciprocating motion between electrodes A and C, the changes in the voltages of these electrodes are not monotonic, and their voltage fluctuations have a clear sawtooth shape. A similar sawtooth shape with a much smaller amplitude is also observed in the induced voltages of electrodes B and D.

Here, we sum the induced voltages of all the electrodes to calibrate the cable voltage. The result is shown in Fig. 8. It can be seen that the fluctuation (peak-to-peak value) of the calibrated cable voltage is more than 25 V and the maximum measurement error is about 15.4%. Table 2 shows the calculated output characteristics of the sensor at different voltages. The fluctuations of the measured voltage all exceed 20 V and the average sensing error exceeds 15%. The voltage fluctuations and sensing errors are mainly due to changes in cable location. The change in the spatial relative location of the cable has a great impact on the sensing performance. It is necessary to perform correlation analysis between the changes in cable spatial location and the induced voltages from the electrode array, and spatially dependent voltage compensation must be applied to the contactless sensor. By analyzing the curves in Fig. 7, a strong correlation is
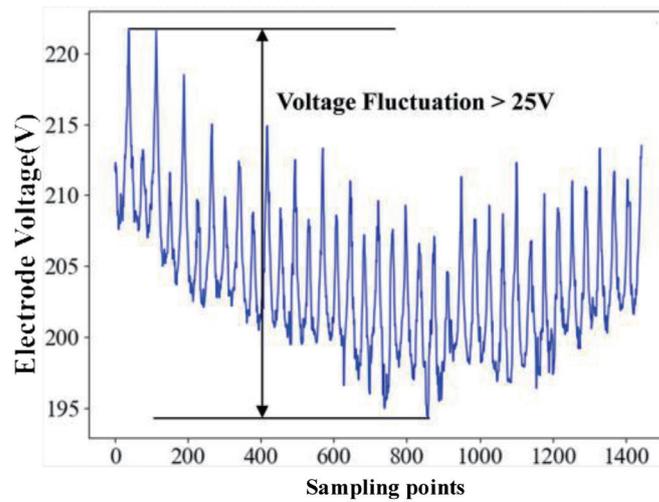
Fig. 8.   (Color online) Change in sensing voltage when cable moves along the path.

Table 2
Voltage fluctuations and errors at different cable voltages.

Actual cable voltage (V)	Voltage fluctuation (V)	*RMS* (V)	Error (%)
160	>25	131	18.1
180	>23	151	16.1
200	>25	169	15.5
220	>27	185	15.9
240	>25	203	15.4

found between the cable location and the induced voltages. When the cable is closer to one of the electrodes, the corresponding induced voltage is larger. If the variations of the induced voltage are collected by the spatially distributed electrode array, by applying suitably designed data training and learning, the collected induced voltage data can indirectly reflect the cable location, and spatially dependent voltage compensation can be performed to increase the accuracy and reliability of sensing.

4.   Principle of Compensation

The principle of the adaptive compensation for the contactless voltage sensor is shown in Fig. 9. The collected cable voltage and the induced voltage of the electrode array are sent to the data processing module. The processed data are applied to the data learning and training module. Voltage compensation is then implemented in the output module. The voltage compensation must be conducted online with the hardware embedded in the sensor, placing limitations on the computational resources. To balance the compensation accuracy and the simplicity of the calculation, a linear regression algorithm with the following equation is adopted in the compensation:
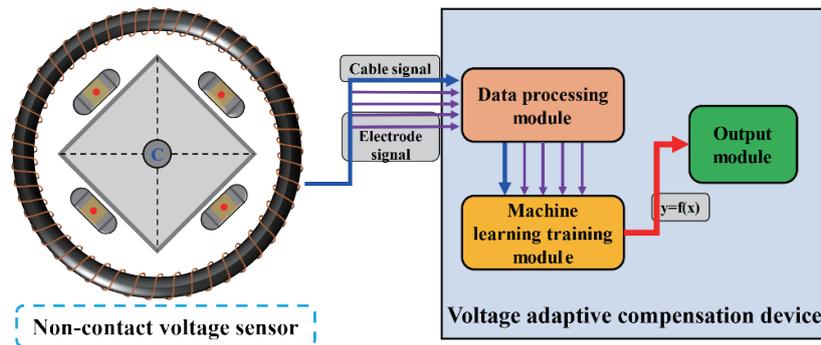
Fig. 9.   (Color online) Principle of adaptive compensation for contactless voltage sensor.

$$y(w,x) = b + w_1 x_1 + w_2 x_2 + \cdots + w_p x_p , \tag{5}$$

where y is the reference voltage, x denotes an eigenvalue, w denotes a compensation coefficient, and b is the error term used to represent the regression error. The coefficient matrix and the corresponding intercept are calculated by the least-squares method to minimize the cost function L defined as

$$L = \sum_{i=1}^{n} (WX_i + b - y_i)^2 , \tag{6}$$

where X_i are eigenvectors and W is the corresponding compensation coefficient matrix. The partial derivatives of $L(W, b)$ with respect to W and b are respectively used to calculate the optimal solutions of W and b to obtain the voltage compensation model.

A flow chart of the training model for voltage compensation is shown in Fig. 10. Firstly, using the setup to measure the sensor characteristics, a data set including the correlation characteristics between the induced voltages of the electrodes and the cable position is collected. Secondly, data analysis and data cleaning are performed. Then, the whole data set is divided into two parts: the training set and test set. Lastly, the training model is used to establish the dependence of the cable voltage y on the eigenvector X_i.

In addition to selecting the induced voltages of the four electrodes, v_A, v_B, v_C, and v_D, as the basic feature values to increase the compensation accuracy, we also include several more dependent variables as additional features such as the square of each electrode voltage and the products of pairs of electrode voltages. The input features applied to the training model are v_A, v_B, v_C, v_D, v_A^2, v_B^2, v_C^2, v_D^2, v_{AB}, v_{AC}, v_{AD}, v_{BC}, v_{BD}, and v_{CD} corresponding to eigenvalues x_1, x_2, x_3, …, x_{14}. The voltage output model can be expressed as
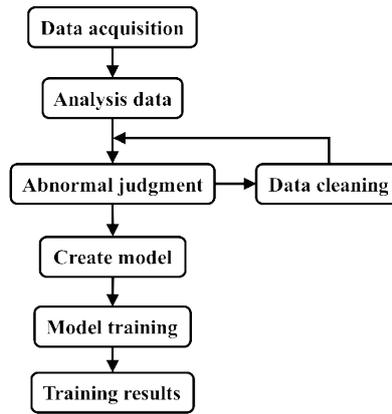
$$Y(W,X) = b + W^T X , \tag{7}$$

Fig. 10.　(Color online) Flow chart of training model for voltage compensation.

where the compensation matrix is $W = [w_1 \quad \cdots \quad w_{14}]^T$ and the eigenvector matrix is $X = [x_1 \quad \cdots \quad x_{14}]^T$.

　　The residual error (*RE*) and mean absolute error (*MAE*) are respectively used to evaluate the accuracy of a single measurement and the overall accuracy. Here, *RE* is defined as

$$e_r = u_i - u_{real}, \tag{8}$$

$$\begin{cases} e_+ = \max\{e_r\} & e_r > 0 \\ e_- = \min\{e_r\} & e_r < 0 \end{cases}, \tag{9}$$

where u_{real} is the cable voltage, e_+ is the positive maximum value of the *RE*, and e_- is the negative minimum value of the *RE*.

　　The *MAE* is defined as

$$MAE = \frac{1}{n}\sum_{i=1}^{n}|u_i - m|, \tag{10}$$

where u_i is the cable voltage measured by the sensor, *m* is the cable voltage, and *n* is the number of sampling points.

5.　Verification of Compensation Algorithm

5.1　Model training of two different data grouping methods

　　When performing model training, the data set must be grouped into a test set and a training set. The grouping method affects the performance of model training. The impact of two different data grouping methods, types A and B, on the voltage measurements is studied.

For type A (Fig. 11), all the test data corresponding to different voltages are first mixed together without marking the voltage labels. Then, 70% of the mixed data are randomly selected as the training set and the remaining 30% are selected as the test set.

For type B (Fig. 12), the cable voltage is measured twice at the same voltage level. The collected data of the first measurement are taken as the training set, and those of the second measurement are taken as the test set. The model training results corresponding to types A and B are respectively

$$Y_A = 32.028 + W_A^T X , \tag{11}$$

$$Y_B = 40.382 + W_B^T X . \tag{12}$$

The compensation coefficient matrices W_A and W_B are shown in Table 3. A comparison of voltage sensing based on the two data groupings for the five different voltages in the range of 160–240 V is shown in Fig. 13. The *x*-axis represents the sampling points on the path of the cable shown in Fig. 5. The *RE* values calculated from Eqs. (8) and (9) are shown in Table 4 and the *MAE* distributions calculated from Eq. (10) are shown in Fig. 14.
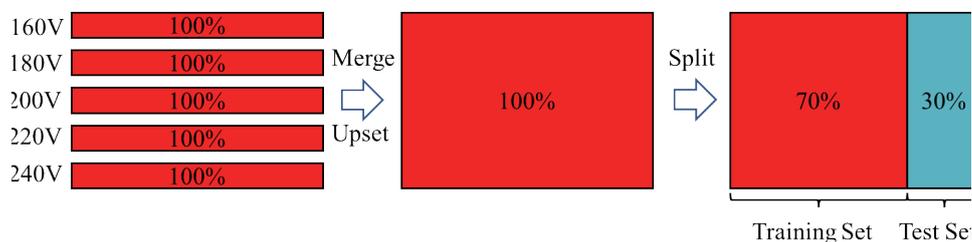

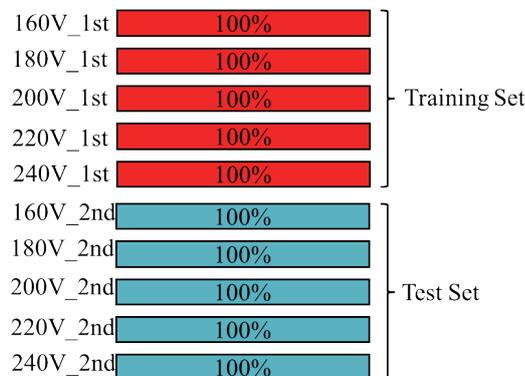Fig. 11.   (Color online) Type A data grouping.

Fig. 12.   (Color online) Type B data grouping.

Table 3
Compensation coefficient matrices W_A and W_B.

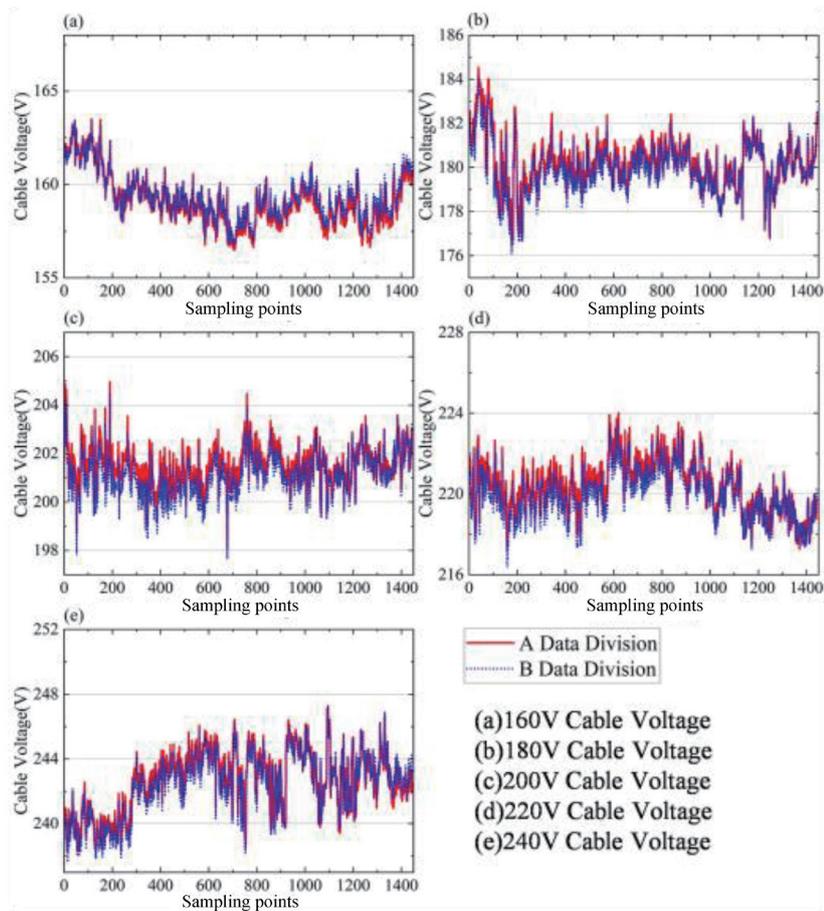| Characteristic value x	W_A for type A data division	W_B for type B data division
x_1	0.244	0.240
x_2	1.336	1.132
x_3	0.263	0.291
x_4	1.570	1.355
x_5	−0.126	−0.138
x_6	−1.129	−1.135
x_7	−0.126	−0.138
x_8	−0.130	−0.142
x_9	0.221	0.240
x_{10}	−0.164	−0.179
x_{11}	0.220	0.246
x_{12}	0.220	0.239
x_{13}	−0.185	−0.214
x_{14}	0.219	0.244

Fig. 13.   (Color online) Comparison of voltage sensing based on type A and B data groupings.

Table 4
RE values of type A and B data groupings.

Cable voltage (V)	Type A		Type B	
	Max. error (V)	Min. error (V)	Max. error (V)	Min. error (V)
160	2.67	−3.73	1.62	−4.97
180	3.35	−3.81	4.18	−4.20
200	2.52	−4.26	2.96	−3.77
220	3.68	−3.96	2.95	−4.89
240	4.55	−4.37	5.24	−2.60
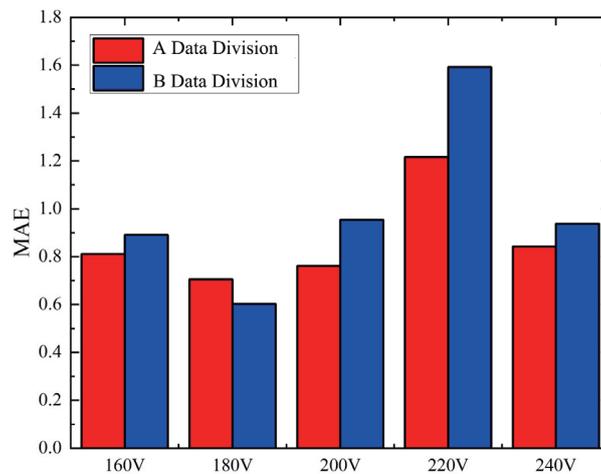
Fig. 14.   (Color online) MAE distributions for voltage compensation based on type A and B data groupings.

Figure 13 shows that both groupings are effective for stabilizing the sensing results; the voltage fluctuations due to changes in location observed in Fig. 7 have been compensated for. The *RE* values shown in Table 4 demonstrate that the maximum error is within 5.3 V, which is much smaller than the errors before compensation. The compensation performance is very similar for the two groupings and it is difficult to identify a difference in performance from Fig. 13. The further comparisons shown in Table 4 and Fig. 14 demonstrate that different data groupings have some impact on the final sensing accuracy, but the impact is relatively small. The average *MAE* values corresponding to types A and B are 0.87 and 0.99, respectively. The type A data grouping results in 12% lower average sensing error, showing its superiority over type B.

5.2   Analysis of compensation performance

The type A data grouping method is selected for data training, and the contactless sensing performance is investigated before and after compensation at *RMS* values of the cable voltage of 160, 180, 200, 220, and 240 V. During the sensing analysis, the cable moves along the path shown in Fig. 5 and the final results are shown in Fig. 15. The *RE* values of the voltage sensing before and after compensation are illustrated in Fig. 16.
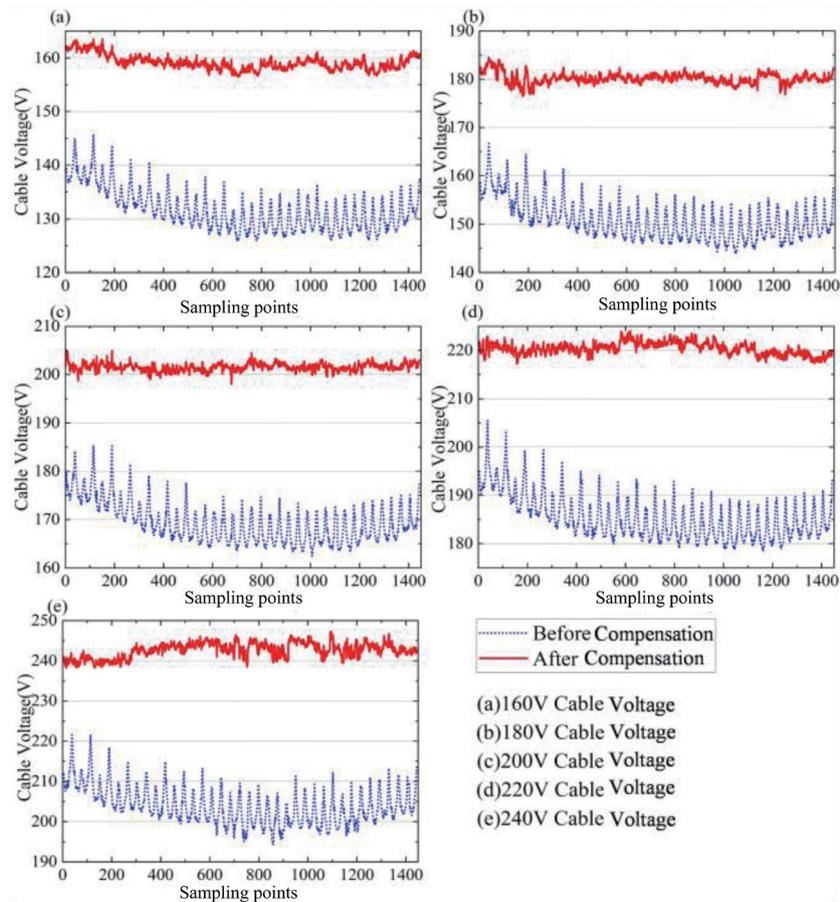
Fig. 15.   (Color online) Comparison of voltage sensing before and after compensation.
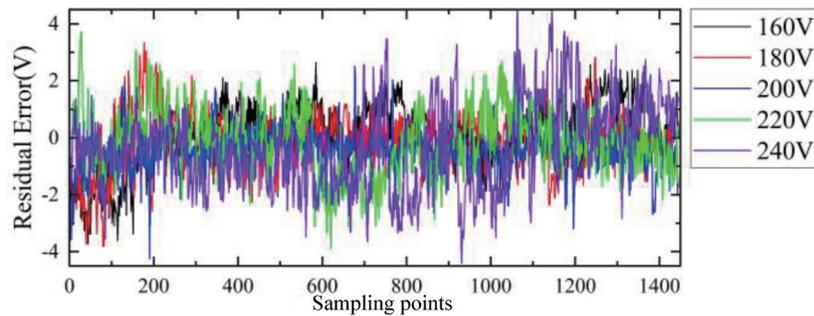

Fig. 16.   (Color online) Comparison of error before and after compensation at different voltages.

Figures 15 and 16 show that without compensation, the sensing accuracy is greatly affected by the position of the cable. The maximum voltage fluctuation exceeds 25 V. The proposed compensation strategy can adaptively compensate for sensing errors resulting from cable movement. It can be seen from Fig. 15 that the sensing results remain almost constant along the

entire path of the cable regardless of the voltage. The *RE* analysis (Fig. 16) shows that for the five cable voltages, the *RE* is limited to ±4 V and all sensing errors are less than 2.5%.

6. Conclusions

(1) To achieve contactless voltage sensing with high accuracy and reliability, an electrode array with four evenly spaced electrodes is designed to detect the spatially distributed electric field resulting from a power cable. A setup for measuring sensor output characteristics is designed to test and analyze the correlation between the sensor output and the change in the relative location of the cable. Results show that the sensor output is greatly affected by the position of the cable. The maximum voltage fluctuation exceeds 25 V.

(2) Adaptive online voltage compensation based on a linear regression algorithm to compensate for the sensing error resulting from changes in cable location is proposed. The compensation results are verified at voltages ranging from 160 to 240 V. It is shown the voltage fluctuation is reduced from ±25 to ±4 V and the maximum sensing error is reduced from 15% to less than 2.5% as a result of adaptive compensation.

References

1   D. Lawrence, J. S. Donnal, and S. Leeb: IEEE Sens. J. **16** (2016) 6095. https://doi.org/10.1109/JSEN.2016.2574245
2   P. Pai, L. Chen, F. K. Chowdhury, and M Tabib-Azar: Sensors (IEEE, 2012) 1–4. https://doi.org/10.1109/ICSENS.2012.6411383
3   R. Zeng, B. Wang, Z. Yu, and W. Chen: IEEE Trans. Dielectr. Electr. Insul. **18** (2011) 312. https://doi.org/10.1109/TDEI.2011.5704523
4   F. Rahmatian and A. Ortega: 2006 IEEE/PES Transmission & Distribution Conference and Exposition: Latin America (IEEE, 2006) 1–4. https://doi.org/10.1109/TDCLA.2006.311482
5   I. A. Metwally: IEEE Trans. Instrum. Meas. **59** (2010) 2211. https://doi.org/10.1109/TIM.2009.2030928
6   M. A. Haberman and E. M. Spinelli: IEEE Trans. Instrum. Meas. **69** (2020) 2790. https://doi.org/10.1109/TIM.2019.2926877
7   M. A. Haberman and E. M. Spinelli: IEEE Trans. Instrum. Meas. **67** (2018) 1946. https://doi.org/10.1109/TIM.2018.2809079
8   W. A. Stygar, H. C. Ives, T. L. Gilliland, R. B. Spielman, M. F. Johnson, P. G. Reynolds, J. K. Moore, R. L. Mourning, D. L. Fehl, K. E. Androlewicz, J. E. Bailey, R. S. Broyles, T. A. Dinwoodie, G. L. Donovan, M. E. Dudley, K. D. Hahn, A. A. Kim, J. R. Lee, R. J. Leeper, G. T. Leifeste, J. A. Melville, J. A. Mills, L. P. Mix, W. B. S. Moore, B. P. Peyton, J. L. Porter, G. A. Rochau, G. E. Rochau, M. E. Savage, J. F. Seamen, J. D. Serrano, A. W. Sharpe, R. W. Shoup, J. S. Slopek, C. S. Speas, K. W. Struve, D. M. Van De Valde, R. M. Woodring, and T. C. Wagoner: Phys. Rev. ST Accel. Beams. **11** (2008) 100401. https://doi.org/10.1103/PhysRevSTAB.11.100401
9   I. A. Metwally: Proc. 1995 Conf. Electrical Insulation and Dielectric Phenomena (IEEE, 1995) 298–301. https://doi.org/10.1109/CEIDP.1995.483722
10 N. Dehghan and S. C. Cripps: IEEE MTT-S Int. Microwave Symp. (2015) 1–3. https://doi.org/10.1109/MWSYM.2015.7166745
11 R. Hou, M. Spirito, F. Van Rijs, and L. C. N. de Vreede: IEEE Microwave Wireless Compon. Lett. **26** (2016) 1008. https://doi.org/10.1109/LMWC.2016.2623250

12   D. Brunelli, C. Villani, D. Balsamo, and L. Benini: Microsyst. Technol. **22** (2016) 1915. https://doi.org/10.1007/s00542-016-2890-7

13   R. Moghe, A. R. Iyer, F. C. Lambert, and D. M. Divan: IEEE Trans. Smart Grid **5** (2014) 2002. https://doi.org/10.1109/TSG.2014.2304533.

14   T. Kubo, T. Furukawa, H. Itoh, H. Fukumoto, and H. Wakuya: 2011 SICE Annual Conf. (SICE) (2011) 2741–2746. https://www.researchgate.net/publication/261277399_Numerical_electric_field_analysis_of_power_status_sensor_observing_power_distribution_system_taking_into_account_measurement_circuit_and_apparatus

15   D. Borkowski, A. Wetula, and A. Bien: IEEE Trans. Smart Grid **6** (2015) 1560. https://doi.org/10.1109/TSG.2014.2363294

16   K. M. Tsang and W. L. Chan: Sens. Actuators, A **167** (2011) 261. https://doi.org/10.1016/j.sna.2011.02.019